Supplementary Information

Dual-control adsorption in hierarchical USY zeolites: orchestrating porosity and hydrophobicity

Jingxuan Wang,[b] Li Li,[b] Lin Li,[a] Conghua Liu,[c] Risheng Bai,*[d] and Pusheng Liu*[a]

Table of Contents

Experimental section

Chemical reagents.

NaY zeolite sample used in this study was provided by Dalian *ZR-Cat Company*. Oxalic acid (>99.5%) was purchased from Innochem Co.

Synthesis of USY samples

Ultra-stable Y (USY) zeolite was prepared by hydrothermally treating commercial NaY at 750 °C for 2 h. The resulting USY was subsequently leached with 0.25 M oxalic acid at 75 °C for 2 h per cycle, using a solid-to-liquid ratio of 1 g : 20 mL. Samples were subjected to different numbers of leaching cycles: USY-1 (1 cycle), USY-2 (3 cycles), USY-3 (5 cycles), and USY-4 (7 cycles). Following leaching, each solid product was filtered, washed with deionized water until neutral pH, and dried at 80 °C for 8 h.

Characterization

X-ray diffraction (XRD)

Powder X-ray diffraction (XRD) data were collected at ambient temperature from 4 to 70° with a step of 0.01° on a *Rigaku* SmartLab SE diffractometer with the Bragg-Brentano geometry, using Cu *Kα* radiation (λ=1.5418Å). The relative crystallinity of the zeolite sample was estimated by comparing total integrated intensity of 12 selected peaks of the sample with that of the reference zeolite Y, according to the method proposed by the *Joint Committee of Powder Diffraction Standard* (JCPDS). The unit cell constant (a_0) was determined by X-ray diffraction method, using high purity silicon powders (99.99 wt %, 25 μm, *High Purity Chemical Laboratory*, Japan) as the internal standard sample. The chemical compositions of the samples were analyzed by X-ray fluorescence (XRF) spectrometry on a *Rigaku* ZSX-Primus IV spectrometer. Bulk *SAR* was also determined via inductively coupled plasma-optical emission spectrometry

(ICP-OES) analysis on an *Agilent* ICP-OES 725 ES.

Structure Refinement

The high-resolution synchrotron XRD pattern of USY-3 was fitted by the least squares method using the program *GSAS&EXPGUI*.[1,2] Synchrotron X-ray diffraction was performed at the high-resolution beamline ID31 at the *European Synchrotron Radiation Facility* (*ESRF*). The sample powder was loaded into a cylindrical slot (approx. 1 mm thickness) held between Kapton windows in a high-throughput sample holder. The sample was measured in transmission with an incident X-ray energy of 75.051 keV (λ = 0.1652 Å). Measured intensities were collected using a *Pilatus* CdTe 2M detector (1679 × 1475 pixels, 172×172 μm^2 each) positioned with the incident beam in the corner of the detector. The sample-to-detector distance was approximately 1.5 m for the high-resolution synchrotron X-ray diffraction measurement. Background measurements for the empty windows were measured and subtracted. NIST SRM 660b (LaB_6) was used for geometry calibration.

Solid-state magic angle spinning nuclear magnetic resonance (MAS-NMR)

The ^{1}H, ^{29}Si, and ^{27}Al solid state MAS NMR experiments were performed at 14.09 T on a *Bruker* Avance NEO 600 spectrometer at resonance frequencies of 600.23, 119.24, and 156.38 MHz, respectively, with a magic angle spinning rate of 8 kHz for 1H and ^{29}Si, as well as 12 kHz for ^{27}Al. Single-pulse ^{29}Si MAS NMR spectra with high power proton decoupling were recorded on a 3.2 mm probe, using a $\pi/2$ pulse of 5.1 μs, a recycle delay of 80 s and 128 scans. The ^{29}Si MAS NMR spectra were referenced to kaolinite (-91.5 ppm). ^{27}Al MAS NMR spectra were acquired on the same 3.2 mm probe by small-flip angle technique with a pulse length of 0.3 μs ($<\pi/12$) and a recycle delay of 0.5 s. The ^{27}Al chemical shifts were referenced to a 1 M Al $(NO_3)_3 \cdot 9H_2O$ solution (0.0 ppm). Single-pulse ^{1}H MAS NMR experiments were performed using a $\pi/2$ ^{1}H pulse length of 4.0 μs, a repetition time of 2 s, and 32 scans. For the two-dimensional (2D) ^{1}H-^{1}H double quantum (DQ) single quantum (SQ) MAS NMR measurements, DQ

coherences were excited and reconverted with a POST-C7 pulse sequence.[1] The increment interval in the indirect dimension was 80 μs. Typically, 128 scans were acquired for each t_1 increment, and two-dimensional data sets consisted of 128 t_1 × 256 t_2. The ^{1}H MAS NMR signals were referenced to adamantane (1.82 ppm).

Fourier Transform infrared spectra (FT-IR)

The infrared (IR) spectra of pyridine adsorbed on the samples were collected on a *Thermo Fisher* Nicolet iS50 spectrometer. Prior to the measurements, samples (~20 mg, pressed into 1.3 cm diameter wafers) were treated under vacuum at 673 K for 1 h. After cooling to ambient temperature, a background spectrum was collected. Pyridine was then introduced until saturation adsorption was achieved. The sample was outgassed for 1 h at 423 K, 523 K and 623 K, and the spectra were recorded after each outgassing step. All spectra were collected at 32 scans and a resolution of 4 cm^{-1}.

The density of Brønsted and Lewis acid sites (C, in mol g^{-1}) was calculated using the equation:

$$C = \frac{A \cdot \pi \cdot R^2}{W \cdot IMEC}$$

where:

A = integrated absorption area

R = radius of the sample wafer (cm)

W = weight of the sample wafer (g)

$IMEC$ = integral molar extinction coefficient.

Scanning electron microscopy (SEM)

Scanning electron microscopy (SEM) images were obtained on a *FEI* Magellan 400 XHR microscope equipped with a cold field emitter as an electron source and an *Everhart–Thornley SE2* detector. The powder sample was initially dispersed in ethanol, and then the suspension was ultrasonicated for 5 minutes before deposited on an aluminium plot. High resolution images were taken at an

accelerating voltage of 2.0 kVor lower by a beam deceleration technique while collecting and mixing secondary-electron and backscatter-electron signals at upper, top, and /or lower detectors.

Transmission electron microscopy (TEM) and scanning TEM (STEM)

Transmission electron microscopy (TEM) and scanning TEM (STEM)-energy-dispersive X-ray spectrometry (EDX) analyses were performed on a *JEOL* JEM-2100F microscope coupled with an X-Max EDS-Detector from *Oxford Instruments*. For the EDS elemental mapping analysis, the accelerating voltage was set at 3.0 kV to detect fluorescence of Si, Al and O.

Argon physisorption

Surface area and porosity of the samples were determined by Ar physisorption at 87.3 K on a *Micromeritics* 3Flex instrument. Before the Ar adsorption/desorption measurements, each sample was degassed at 573 K for 12 h under vacuum. The data were analyzed using the Brunauer-Emmett-Teller (BET), t-plot, α_s-plot and density functional theory (cylinder geometry, NL-DFT) models.

Nitrogen physisorption

Nitrogen adsorption-desorption measurements were carried out on a Micromeritics 3Flex analyzer at 77 K. Before starting the N_2 adsorption measurements, all the samples were activated by degassing in-situ at about 573 K for 12 h. The data were analyzed using the Brunauer-Emmett-Teller (BET), t-plot and density functional theory (cylinder geometry, NL-DFT) models.

Contact angle

The experiment of contact angles was measured on a contact angle meter (DSA100, KRUSS, Germany).

Water adsorption

Water adsorption measurements were carried out on an IGA sorp analyzer at 298 K. Before starting the H_2O adsorption measurements, all the samples were activated by

heating in-situ at about 423 K for 10 h.

Temperature-programmed desorption (TPD)

The experiment of temperature-programmed desorption of H_2O (H_2O-TPD) was measured on a Micromeritics AutoChem II 2920 instrument. For the H_2O -TPD measurements, typically, 100 mg of samples were used for each measurement. The sample was pretreated at 500 °C in an He gas flow for 60 min and then with He gas flow for 30 min.

Vapor Adsorption Experiments

Ca. 100 mg of each sample was loaded into a preweighted sample tube, and the sample tubes were capped with a Transeal equipped with Kalres O-ring. The sample tubes were then transferred to a *Micromeritics* VacPrep 061 instrument and degassed at 573 K for 12 h under vacuum. After activation, the sample tubes were transferred to a *Micromeritics* 3Flex analyzer equipped with a vapor dosing tube for vapor adsorption measurements. The sample tubes were subsequently immersed in a *Micrometrics* ISO Controller. Prior to the measurements, the solvent was degassed on the analyzer via three freeze-pump-thaw cycles. The vapor dosing tube was then heated to 308 K with a heating mantle and maintained at this temperature throughout the experiment. The instrument manifold was heated to 318 K to prevent condensation of the vapor. Adsorption measurements were conducted in fixed incremental dose mode with dosing increments of 1.0 cm^3/g, STP.

Vacuum Static Gravimetric measurement

Vacuum Static Gravimetric measurements were carried out on an Vacuum Vapor/Gas Sorption Analyzer (BSD-VVS). The sample was first degassed at 250 °C for 3 hours, followed by measurement at 45 °C.

Supplementary Figures and Tables

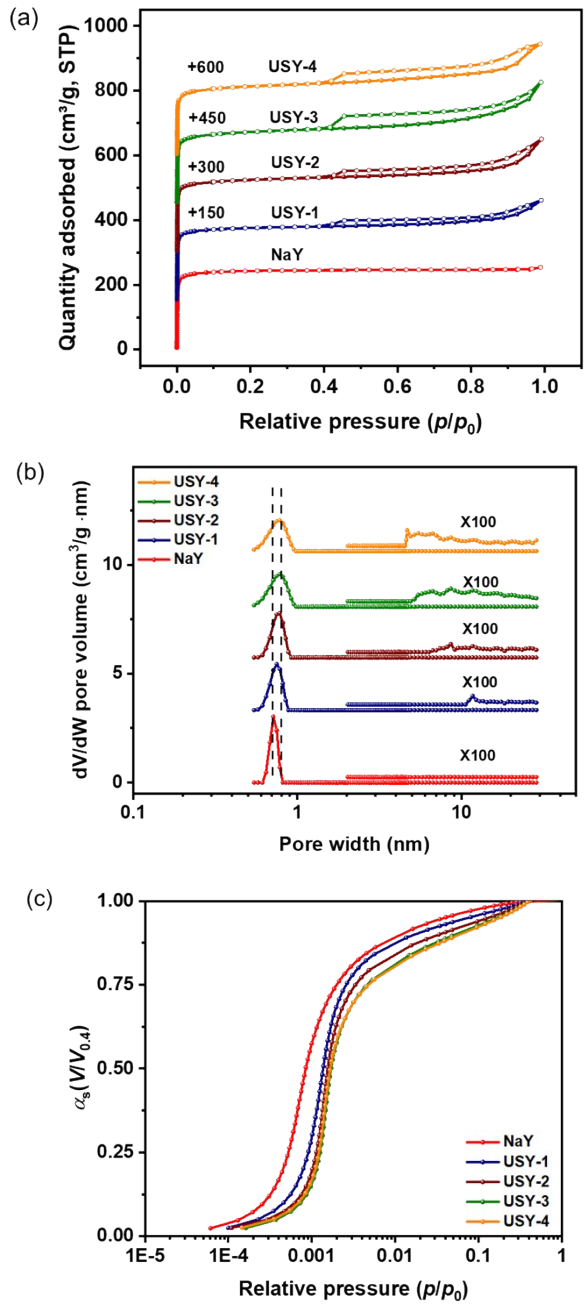

Fig. S1. (a) Ar adsorption/desorption isotherms of the samples measured at 87.3K. (b) NL-DFT pore size distribution of the samples obtained by evaluating Ar physisorption results measured at 87.3K. Pore size distribution curves in the figure have been offset along the vertical axis for clarity. (c) α_s-plots of the zeolite samples on a semilogarithmic scale measured at 87.3 K.

Note: The Ar adsorption–desorption isotherms of NaY zeolite exhibit typical Type I(a) isotherm characteristics: rapid adsorption takes place at extremely low relative pressures (p/p_0) owing to micropore filling, followed by a distinct adsorption plateau within a broad pressure range; the adsorption and

desorption branches are nearly reversible, indicating the absence of considerable mesoporous structures in the sample. For typical microporous zeolites with pore sizes below 1 nm, the adsorption capacity hardly increases further after complete micropore filling, since no additional accessible micropore volume is available. In contrast, the isotherms of USY zeolite samples combine the features of Type I and Type IV isotherms: besides the steep adsorption at very low p/p_0, a pronounced H4-type hysteresis loop emerges in the p/p_0 range of 0.4–1.0, where the adsorption and desorption branches do not coincide. The gradual increase in adsorption capacity and the appearance of the hysteresis loop in this region are ascribed to mesopore filling via multilayer adsorption and capillary condensation of Ar within the mesopores of USY zeolite particles. Moreover, the H4-type hysteresis loop widens markedly with the rise of the silica-to-alumina ratio (SAR), a phenomenon closely correlated with the enhanced dealumination degree during acid leaching.

The pore structural parameters are summarized in Table S3. A clear trend emerges with dealumination: as the SAR increases, the micropore surface area and volume decrease systematically, while the external surface area and mesopore volume increase concurrently. This is exemplified by the contrast between NaY, which possesses the largest micropore surface area (818 $m^2 g^{-1}$) and volume (0.29 $cm^3 g^{-1}$) and the smallest external surface (54 $m^2 g^{-1}$) and mesopore volume (0.04 $cm^3 g^{-1}$), and USY-4, which exhibits the lowest micropore metrics (617 $m^2 g^{-1}$; 0.22 $cm^3 g^{-1}$) alongside the highest external surface area (120 $m^2 g^{-1}$) and mesopore volume (0.22 $cm^3 g^{-1}$). These quantitative results confirm that dealumination transforms the pore architecture, significantly reducing the microporosity while developing a substantial hierarchical mesoporous network.

Ar physisorption analysis clearly demonstrates that NaY zeolite is dominated by microporous structures, which is consistent with its high relative crystallinity and the ordered lattice observed under high-resolution transmission electron microscopy. On the contrary, dealumination leads to a pronounced decrease in the micropore surface area and volume of USY zeolite; this modification process endows USY samples with unique structural features, including tortuous linear morphologies, randomly distributed pits, and hollow internal structures (Fig. 3).

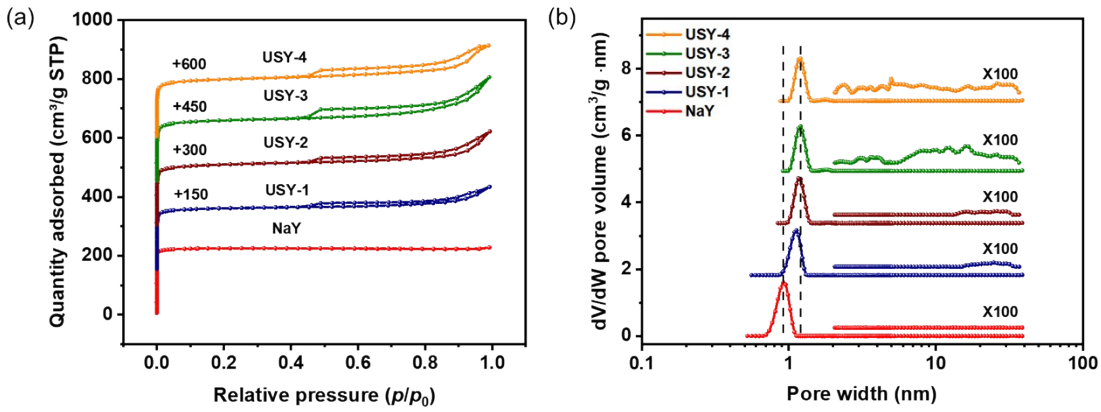

Fig. S2. (a) N_2 adsorption/desorption isotherms of the samples measured at 77 K. (b) NL-DFT pore size distribution of the samples obtained by evaluating N_2 physisorption results measured at 77 K. Pore size distribution curves in the figure have been offset along the vertical axis for clarity.

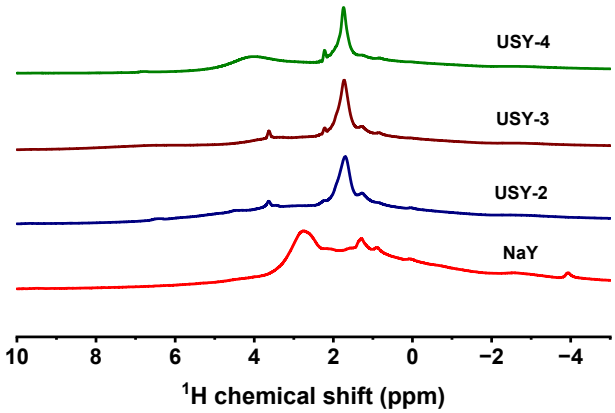

Fig. S3. ^{1}H MAS NMR spectra of the FAU samples.

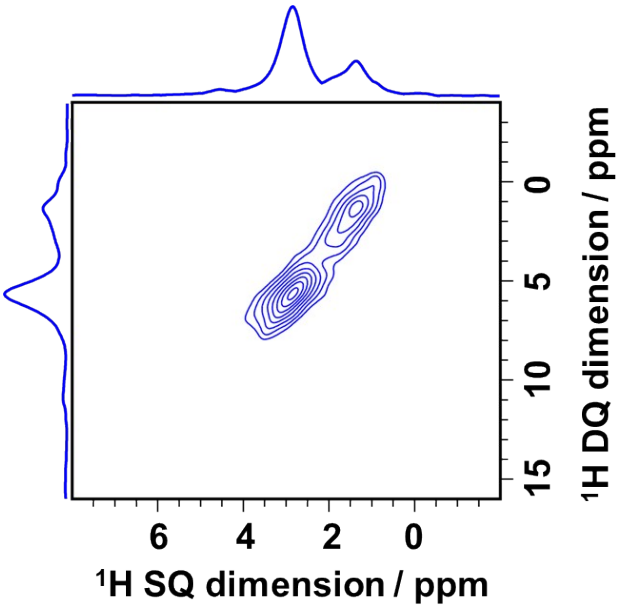

Fig. S4. 2D ^{1}H-^{1}H DQ-SQ spectra of NaY.

Note: The 2D ^{1}H-^{1}H DQ-SQ NMR spectra provide a spatial map of hydroxyl group proximities that evolves systematically with dealumination. In the parent NaY (Fig. S4), correlations are dominated by signals from Si-OH (~1.4 ppm) and Al-OH (~2.7 ppm) species. Upon initial dealumination (USY-2, Fig. S5), the emergence of a clear autocorrelation signal at (3.7, 7.4 ppm) confirms the presence of proximal pairs of Brønsted acid sites (Si-OH-Al), indicative of remaining framework aluminum clusters.

As dealumination proceeds (USY-3, Fig. 2c), the intensity of this Brønsted pair correlation diminishes, reflecting the removal of framework Al and the breaking apart of acid site pairs. Concurrently, the signal for isolated silanols (Si-OH, ~1.8 ppm) becomes more pronounced. In the highly dealuminated USY-4 (Fig. 2d), the Brønsted pair signal disappears entirely, and the spectrum is dominated by silanols.

This progression directly illustrates the chemical transformation of the pore surface: the removal of framework Al eliminates Brønsted acid sites and leaves behind a silanol-rich, increasingly hydrophobic surface. The loss of spatial correlations between acid sites in USY-3 and USY-4 further confirms their isolation within the developing mesoporous structure, which is consistent with the enhanced hydrophobicity and altered VOC adsorption mechanism discussed in the manuscript.

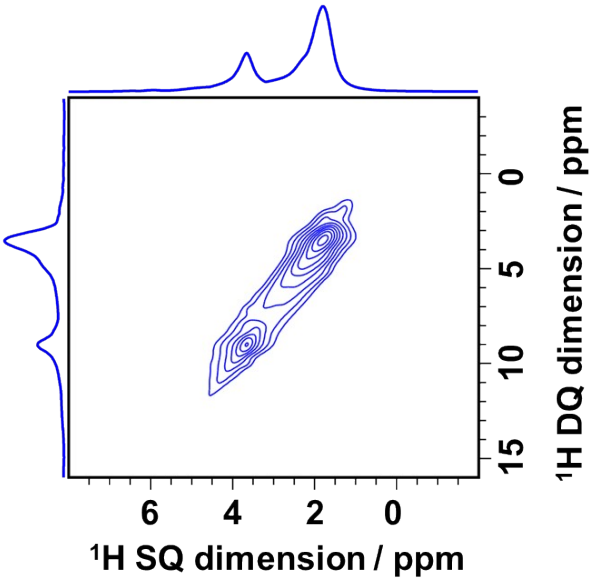

Fig. S5. 2D ^{1}H-^{1}H DQ-SQ spectra of USY-2.

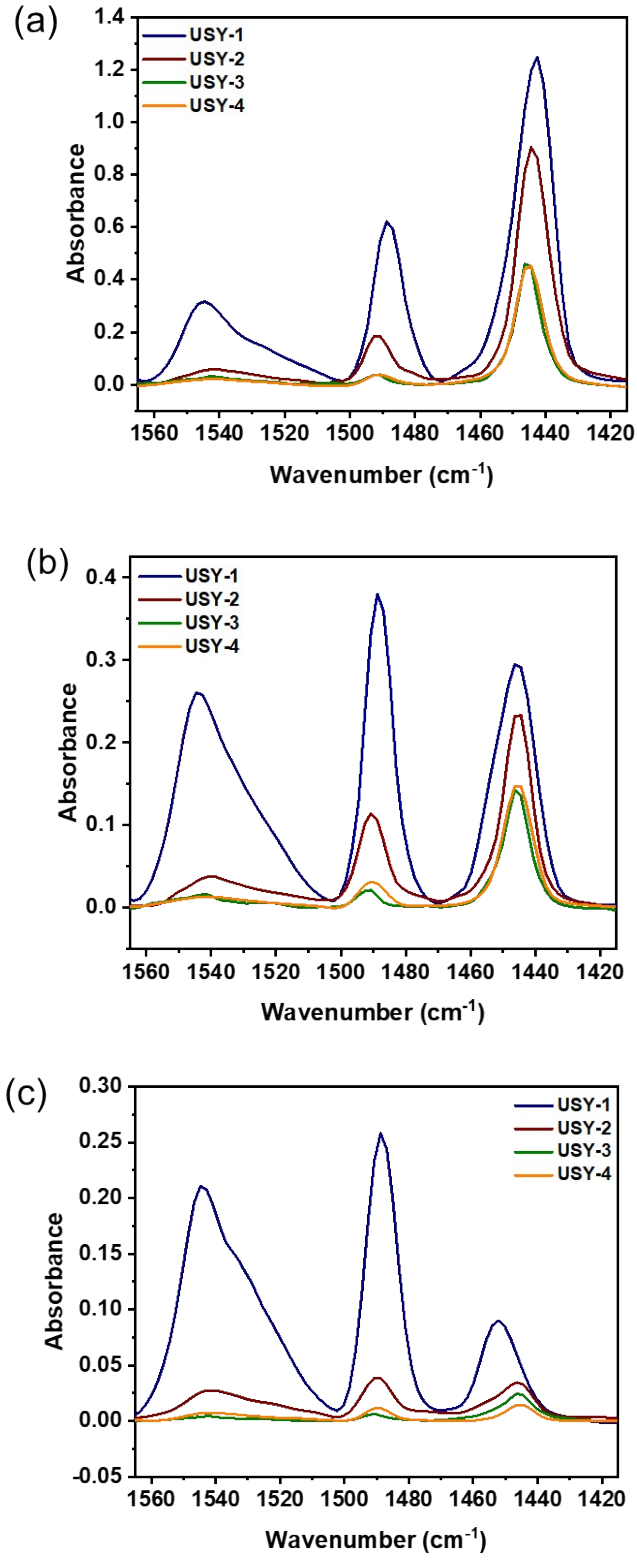

Fig. S6. FT-IR spectra of the pyridine absorbed over the USY samples measured at (a) 423 K, (b) 523 K and (c) 623 K.

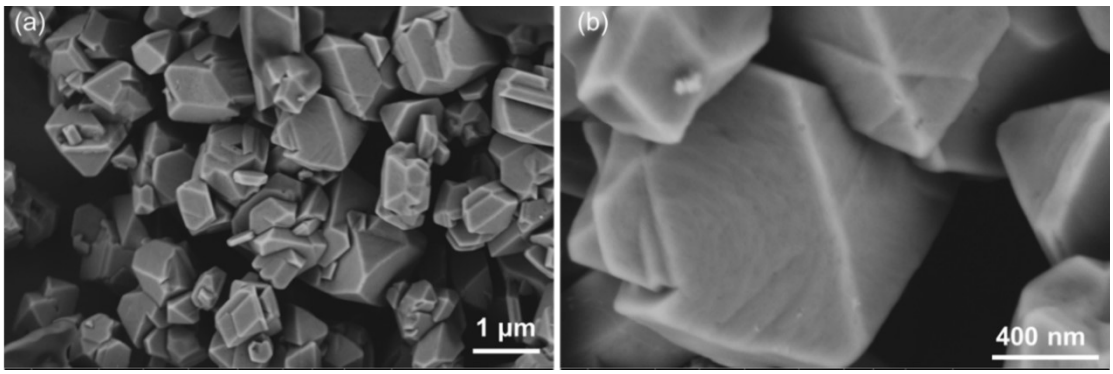

Fig. S7. (a) Low and (b) high magnification SEM images of NaY sample.

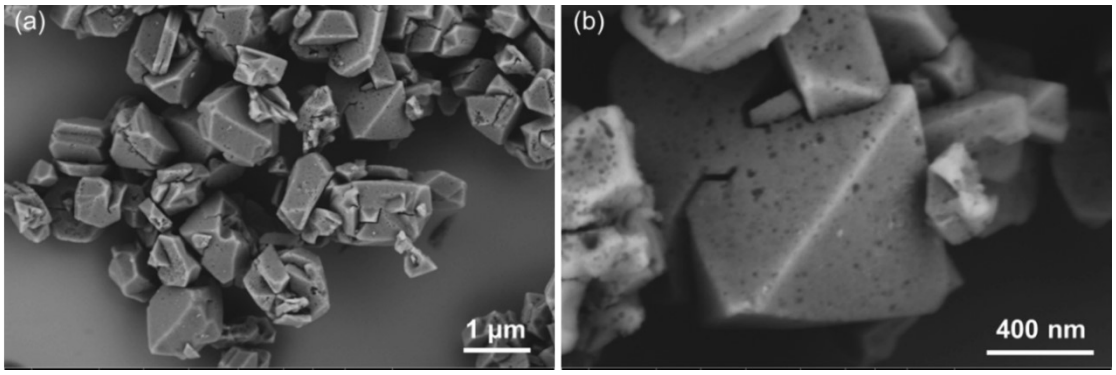

Fig. S8. (a) Low and (b) high magnification SEM images of USY-1 sample.

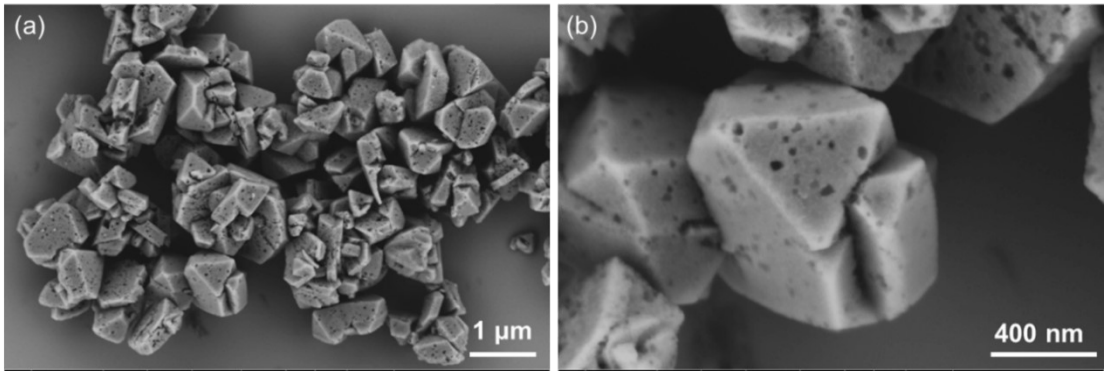

Fig. S9. (a) Low and (b) high magnification SEM images of USY-2 sample.

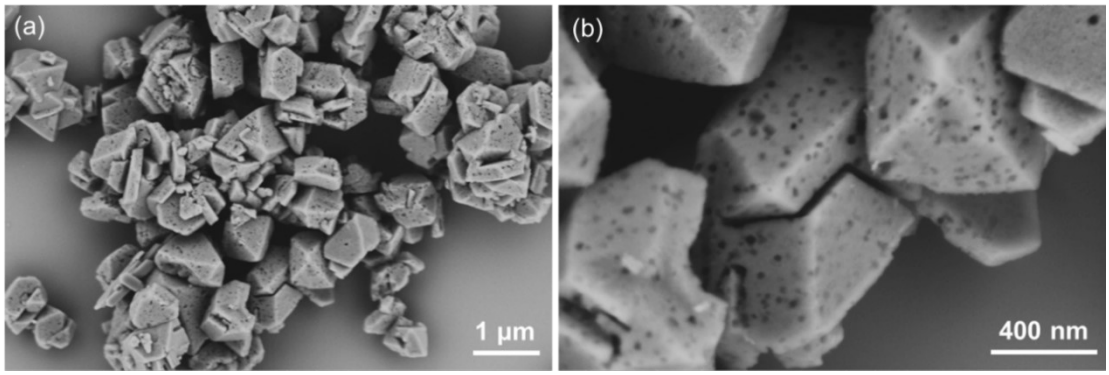

Fig. S10. (a) Low and (b) high magnification SEM images of USY-3 sample.

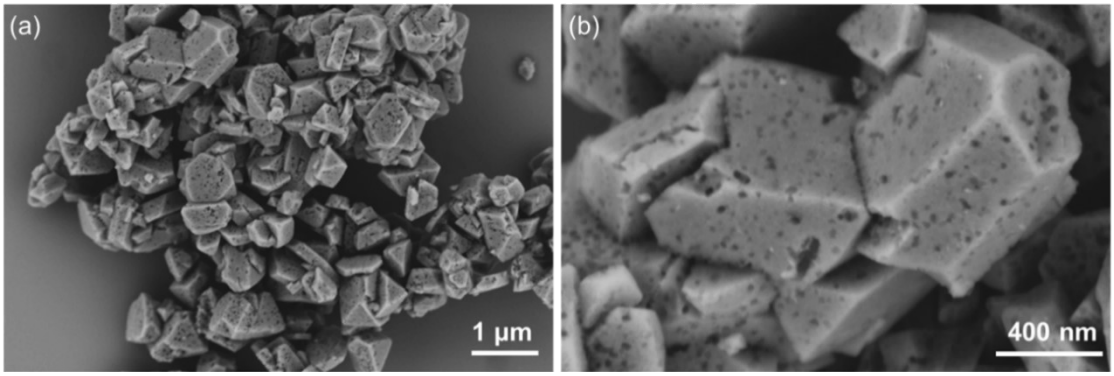

Fig. S11. (a) Low and (b) high magnification SEM images of USY-4 sample.

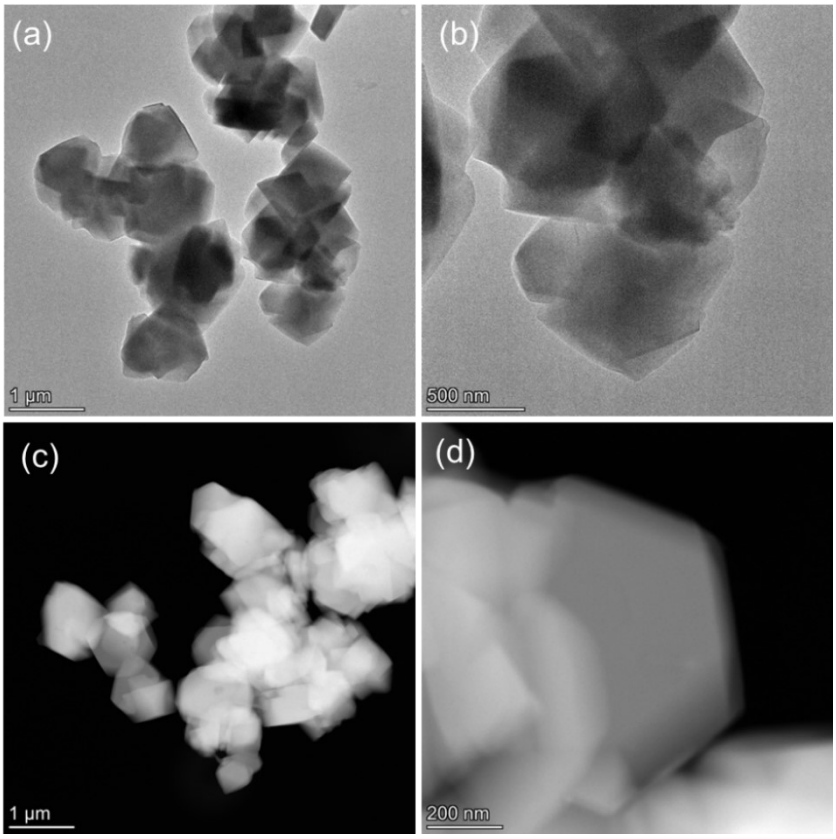

Fig. S12. (a) Low and (b) high magnification TEM images of NaY sample. (c) Low and (d) high magnification STEM-ADF images of NaY sample.

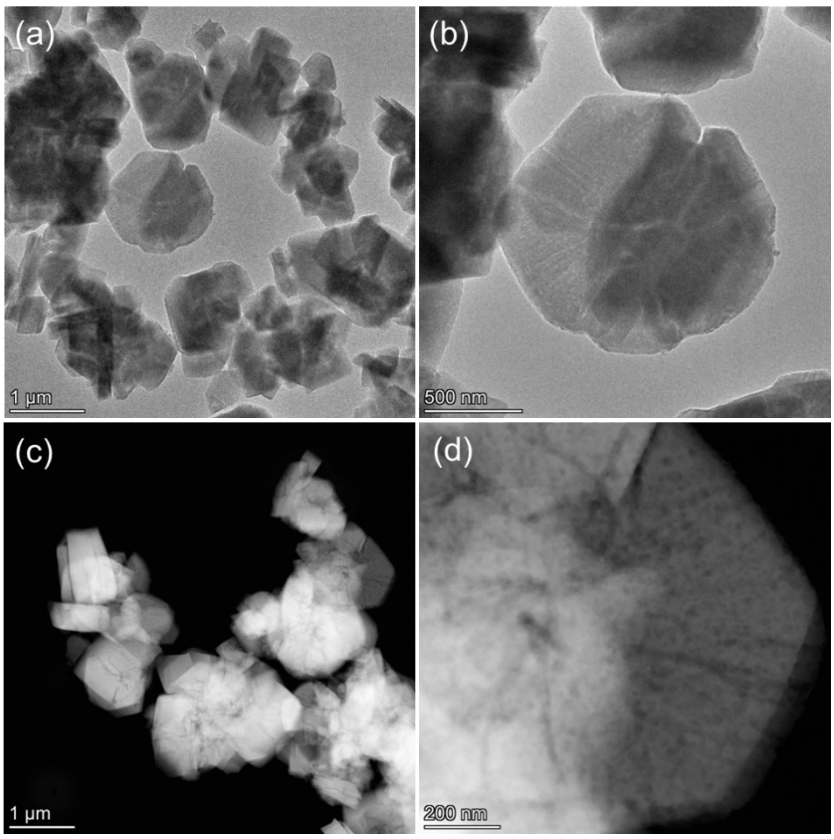

Fig. S13. (a) Low and (b) high magnification TEM images of USY-1 sample. (c) Low and (d) high magnification STEM-ADF images of USY-1 sample.

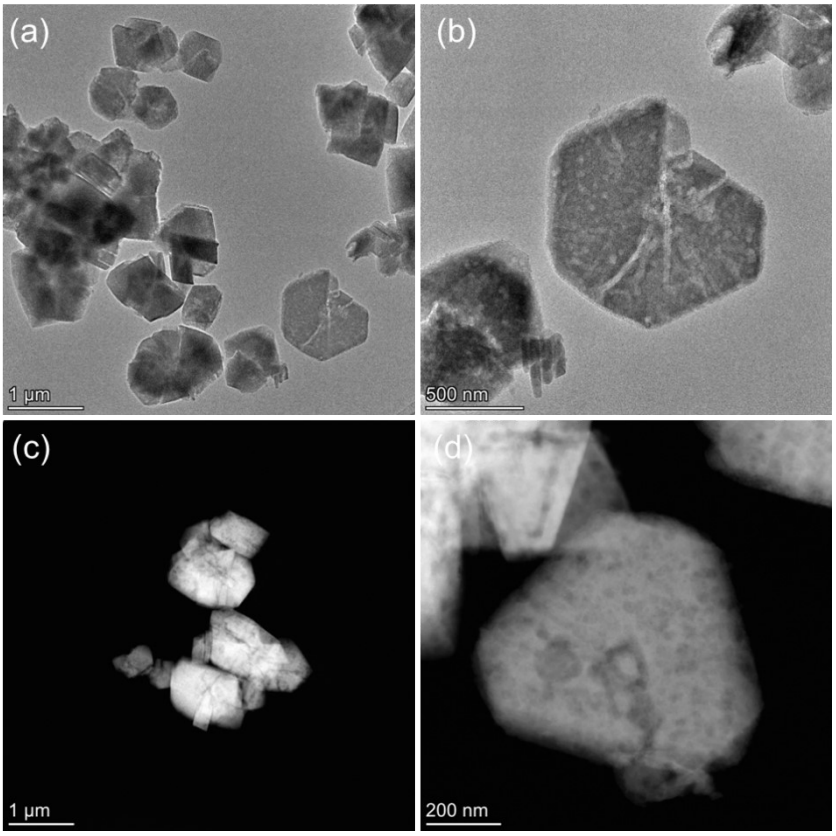

Fig. S14. (a) Low and (b) high magnification TEM images of USY-2 sample. (c) Low and (d) high magnification STEM-ADF images of USY-2 sample.

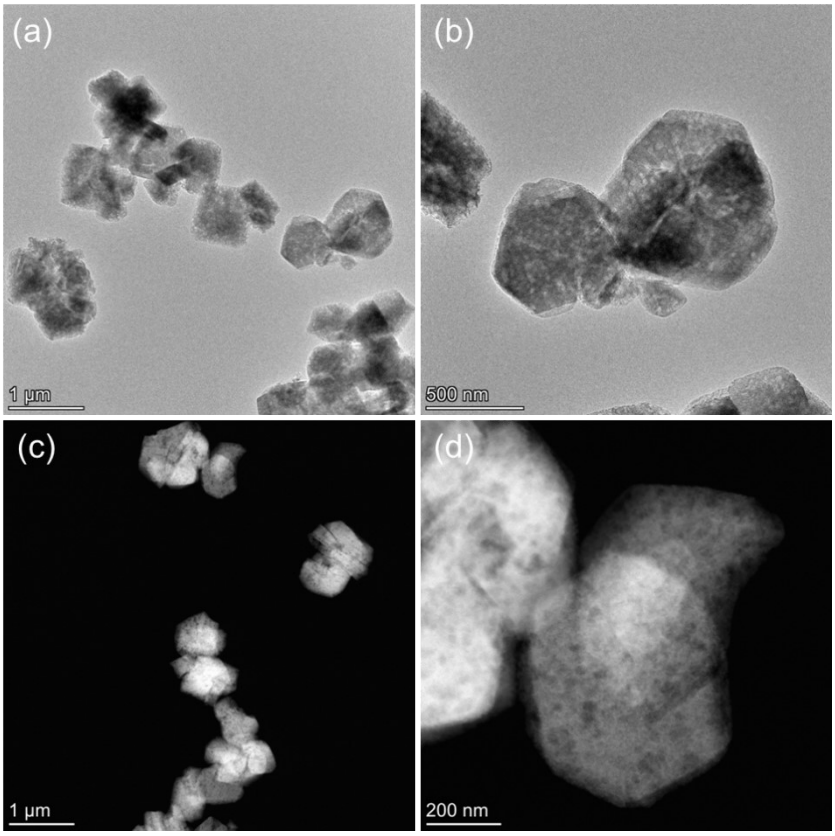

Fig. S15. (a) Low and (b) high magnification TEM images of USY-3 sample. (c) Low and (d) high magnification STEM-ADF images of USY-3 sample.

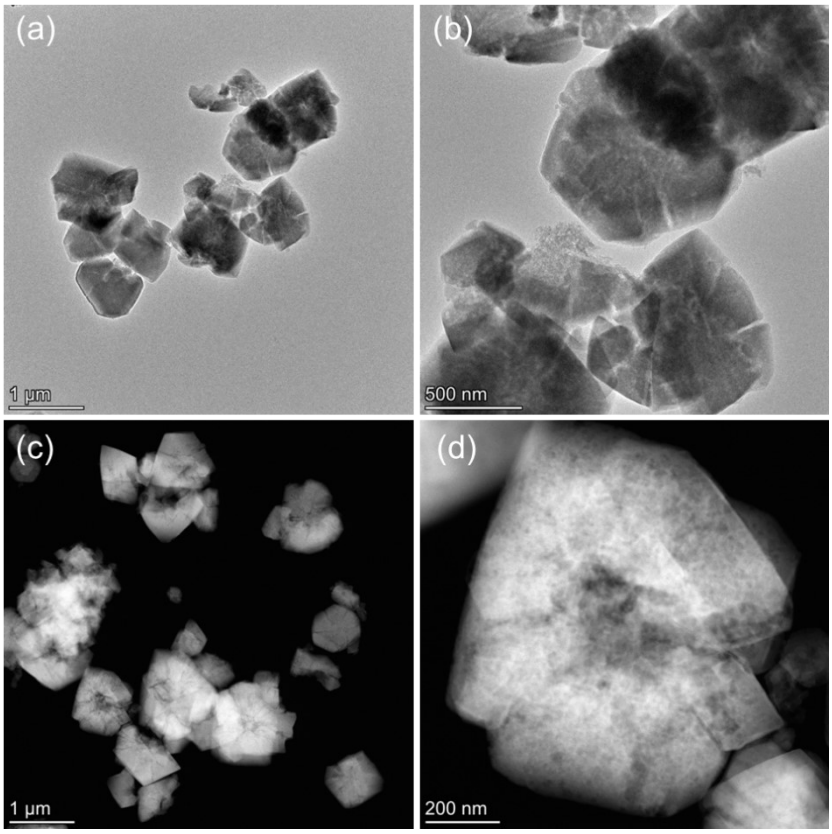

Fig. S16. (a) Low and (b) high magnification TEM images of USY-4 sample. (c) Low and (d) high magnification STEM-ADF images of USY-4 sample.

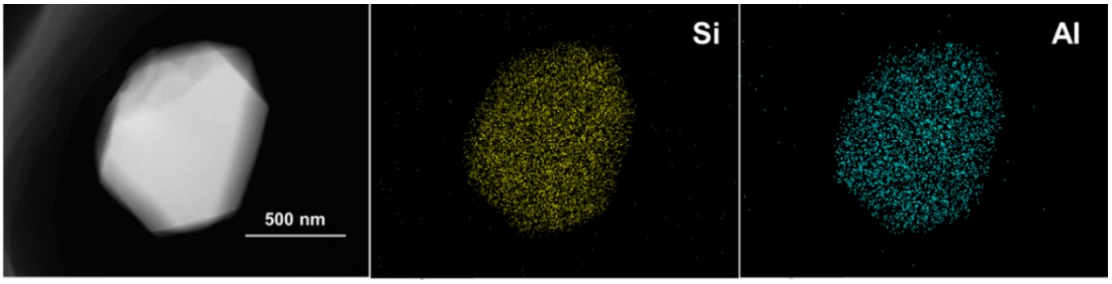

Fig. S17. EDX mapping analysis of NaY.

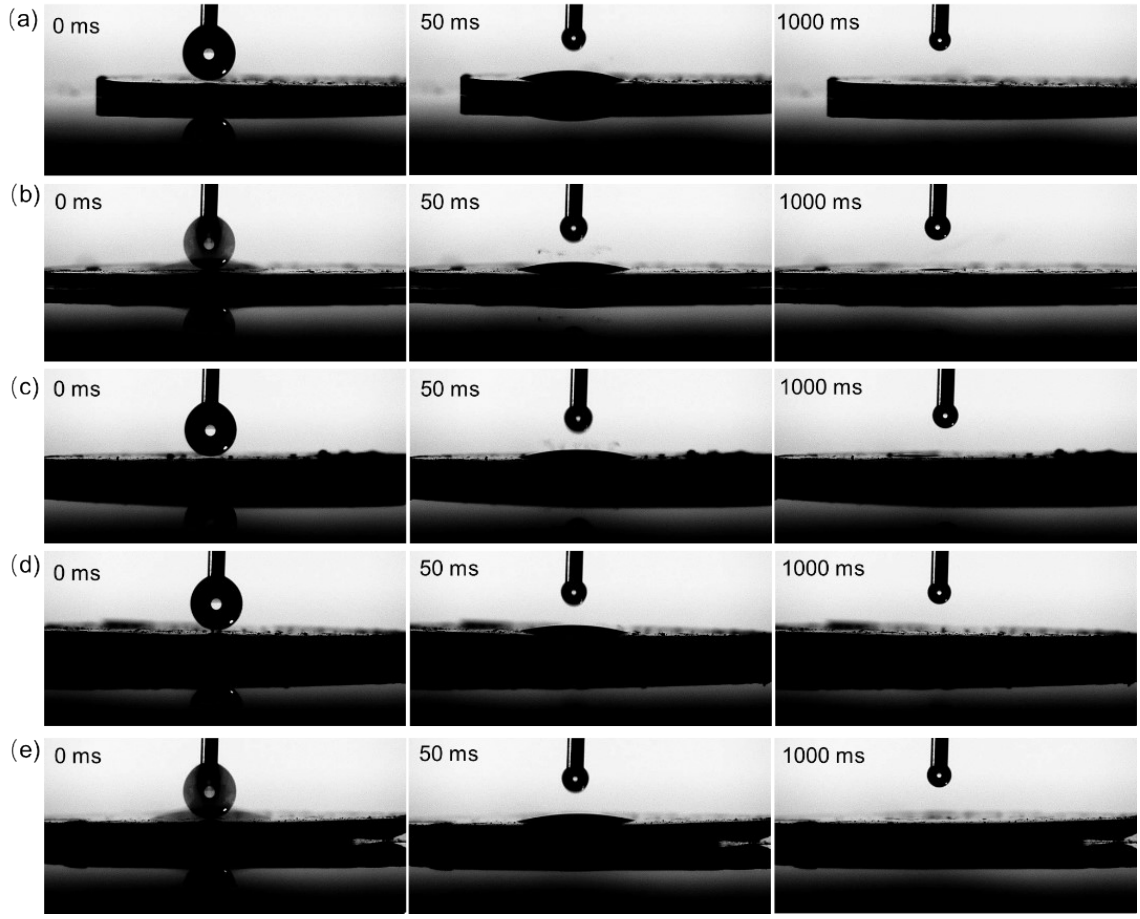

Fig. S18. Water contact angle measurement Images of (a) NaY, (b) USY-1, (c) USY-2, (d) USY-3 and (e) USY-4.

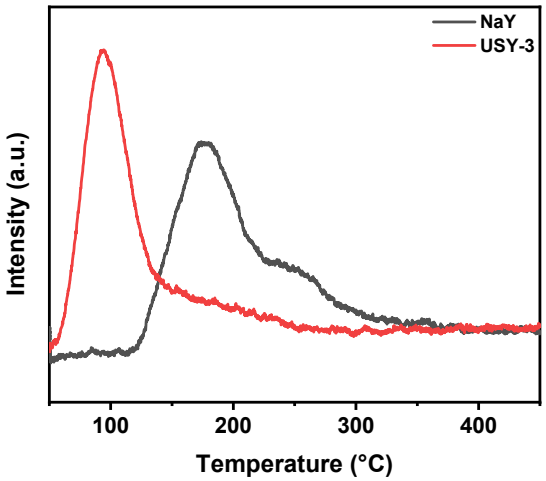

Fig. S19. Water-TPD spectra of NaY and USY-3.

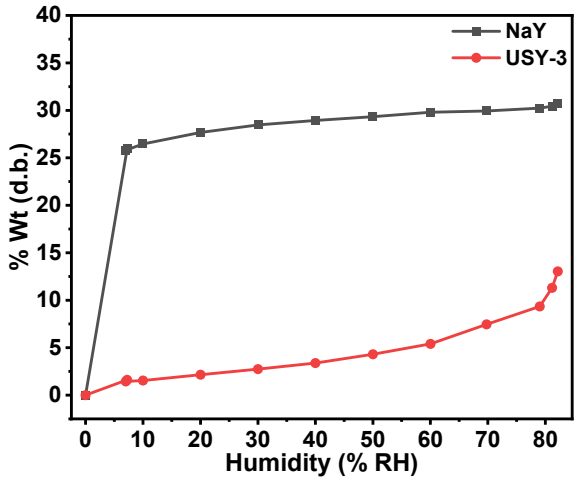

Fig. S20. Water of adsorption isotherms of NaY and USY-3 measured at different hymidity.

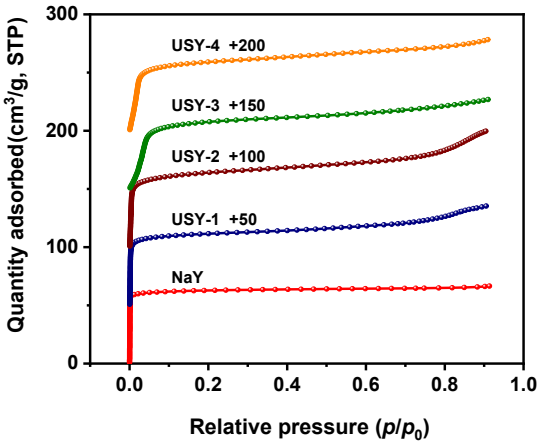

Fig. S21. Toluene vapor adsorption isotherms of the FAU samples measured at 298K.

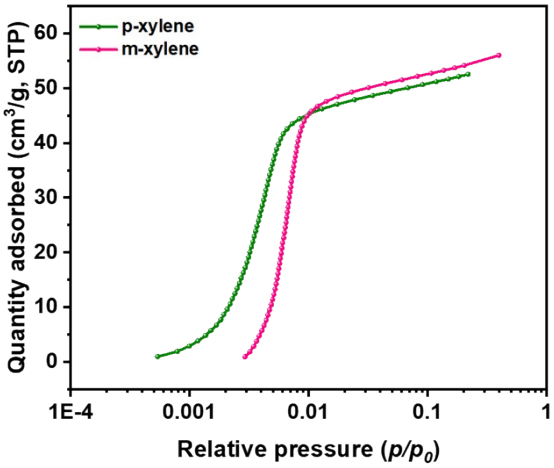

Fig. S22. xylene adsorption isotherms of USY-1 measured at 318 K.

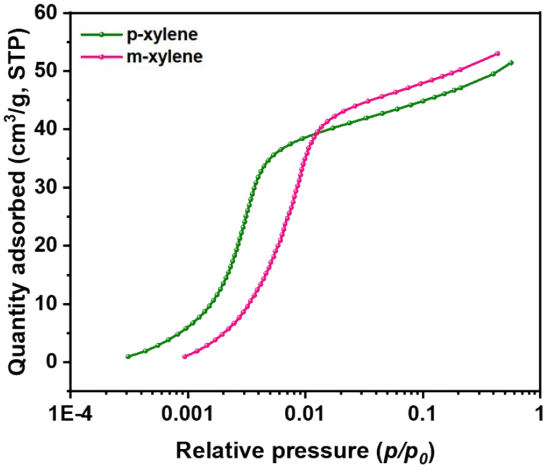

Fig. S23. xylene adsorption isotherms of USY-2 measured at 318 K.

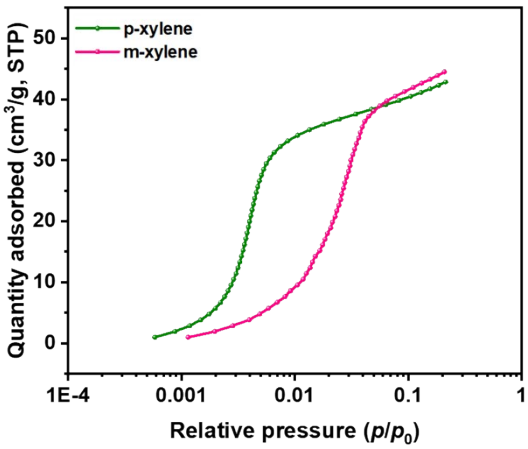

Fig. S24. xylene adsorption isotherms of USY-4 measured at 318 K.

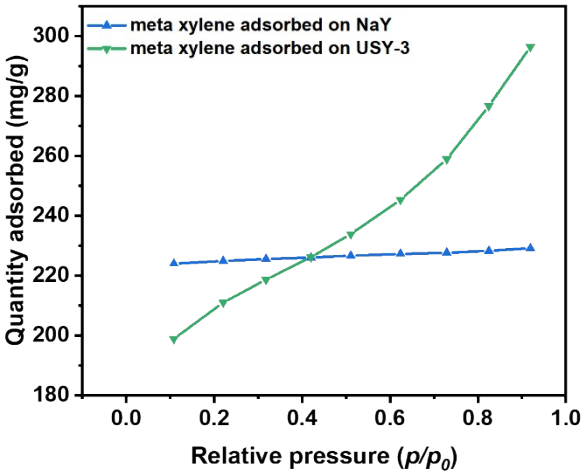

Fig. S25. m-xylene adsorption isotherms of NaY and USY-3 measured at 318 K.

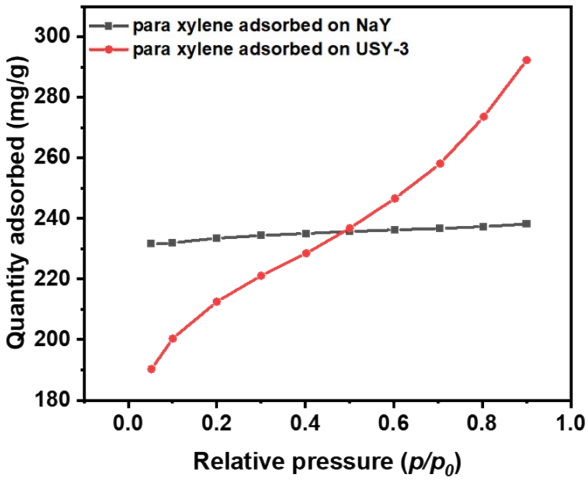

Fig. S26. p-xylene adsorption isotherms of NaY and USY-3 measured at 318 K.

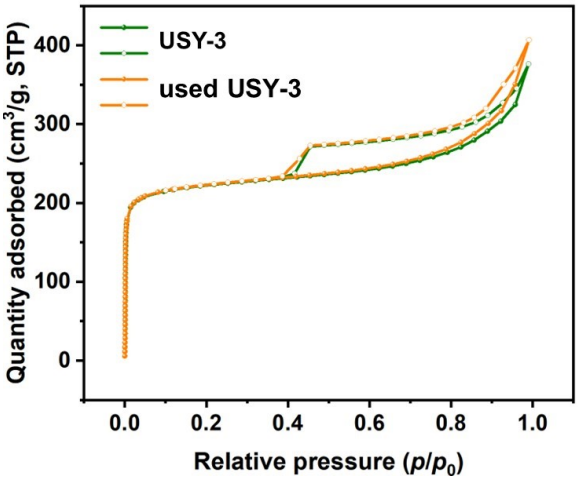

Fig. S27. Ar adsorption/desorption isotherms of the fresh and used USY-3 measured at 87.3 K.

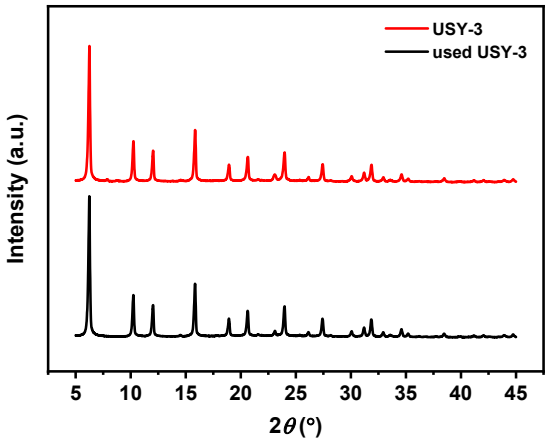

Fig. S28. Powder XRD patterns of the fresh and the used USY-3.

Table S1. Textural properties of the samples

Sample	a_0, angstrom	c/c_0, %	$Na_2O_{XRF,}$ wt%	$Na_2O_{ICP,}$ wt%	SAR_{XRF},	SAR_{ICP},
NaY	24.67	102	11.7	10.7	5.0	5.1
USY-1	24.42	71	0.1	0.1	12.2	14.1
USY-2	24.31	65	0.1	0.1	48.8	55.6
USY-3	24.27	58	0.1	0.1	96.1	93.7
USY-4	24.31	56	0.1	0.1	119.8	115.6

A total of 1140 Bragg reflections were included in the refinements of USY-3. The pattern was refined in the space group $Fd\bar{3}m$ (No. 227), and the atomic coordinates, occupancies (*Occ.*) and temperature parameters (*Uiso*) of T (=Si, Al) atoms were constrained in the initial stage of *Rietveld* refinements. The peak profile and background of diffraction patterns were modeled using a *pseudo-Voigt* function (2 *Gaussian* and 2 *Lorentzian* line-broadening terms) and a shifted *Chebyshev* function (24 terms), respectively. The refinements were successful based on the rationality of atomic parameters, the small residual factors (R) and goodness of fit ($\chi 2$) of the least-squares method.

Table S2. (a) Refined atomic coordinates, occupancies (*Occ*.), temperature parameters (*Uiso*) and unit cell constants (a_0) for USY-3.

Sites		USY-3
T 192(i)	*x*	-0.05425(3)
	y	0.12547(4)
	z	0.03577(4)
	Occ.	0.738
	Uiso ×100 (Å^2)	0.946(0.020)
O1 96(h)	*x*=-*y*	-0.10625(7)
	z	0
	Occ.	0.731(0.004)
	Uiso ×100 (Å^2)	1.469(0.046)
O2 96(g)	*x*=*y*	-0.00353(9)
	z	0.14026(11)
	Occ.	0.723(0.004)
	Uiso ×100 (Å^2)	1.469(0.046)
O3 96(g)	*x*=*y*	0.17392(8)
	z	-0.03661(11)
	Occ.	0.711(0.004)
	Uiso ×100 (Å^2)	1.469(0.046)
O4 96(g)	*x*=*y*	0.17864(8)
	z	0.32004(11)
	Occ.	0.708(0.004)
	Uiso ×100 (Å^2)	1.469(0.046)
Residual factors	*R*wp, %	6.78
	*R*p, %	4.72
	χ2	1.974
a_0(Å)		24.1789(1)

[a] The numbers in parentheses are the esd's in the units of the least significant digit given for the corresponding parameter; in the refinement, the positions of H_2O molecules in the supercages and H element are undetermined.

[b] In the refinement, the occupancy of T atom is fixed; the temperature parameters of T atoms and framework oxygens were constrained at the initial stage of *Rietveld* refinements.

Table S2. (b) Selected bond distances (Å) and angles (°) for USY-3.

Distance	USY-4	Angle	USY-3
T-O1	1.5953(12)	O1-T-O2	110.43(12)
T-O2	1.5921(11)	O1-T-O3	108.85(13)
T-O3	1.5992(11)	O1-T-O4	109.81(14)
T-O4	1.5935(12)	O2-T-O3	109.03(17)
Average	1.5950	O2-T-O4	109.00(15)
T-O1-T	138.85(18)	O3-T-O4	109.71(16)
T-O2-T	150.33(20)	Average	109.47
T-O3-T	147.03(21)	/	/
T-O4-T	144.49(20)	/	/
Average	145.17	/	/

[a] The numbers in parentheses are the esd's in the units of the least significant digit given for the corresponding parameter

Table S3. Pore characteristics of the samples obtained from Ar physisorption isotherms.

sample	S_{BET}[a], m^2/g	S_{micro}[b], m^2/g	S_{ext}[c], m^2/g	V_{total}[d], cm^3/g	V_{micro}[e], cm^3/g	V_{meso}[f], cm^3/g
NaY	872	818	54	0.33	0.29	0.04
USY-1	804	728	76	0.40	0.25	0.15
USY-2	787	686	101	0.45	0.24	0.20
USY-3	771	653	118	0.48	0.23	0.25
Used USY-3	772	647	124	0.51	0.23	0.28
USY-4	737	617	120	0.44	0.22	0.22

[a] Specific surface area (S_{BET}) calculated by the BET method with p/p_0 in the range of 0.005-0.01.[b] Micropore surface area (S_{micro}) calculated by the t-plot method.[c] External surface area (S_{ext})=(S_{BET}–S_{micro}).[d] Total pore volume (V_{total}) estimated by the single point adsorption of pores according to Gurvich rule.[e] Micropore volume (V_{micro}) calculated by the t-plot method.[f] Mesopore volume (V_{meso})=(V_{total}–V_{micro}).

Table S4. Pore characteristics of the samples obtained from N_2 physisorption isotherms.

sample	S_{BET}[a], m^2/g	S_{micro}[b], m^2/g	S_{ext}[c], m^2/g	V_{total}[d], cm^3/g	V_{micro}[e], cm^3/g	V_{meso}[f], cm^3/g
NaY	938	919	19	0.35	0.34	0.01
USY-1	859	797	62	0.44	0.30	0.14
USY-2	836	734	102	0.50	0.28	0.22
USY-3	837	733	104	0.55	0.28	0.28
USY-4	791	683	108	0.49	0.26	0.23

[a] Specific surface area (S_{BET}) calculated by the BET method with p/p_0 in the range of 0.005-0.01.[b] Micropore surface area (S_{micro}) calculated by the t-plot method.[c] External surface area (S_{ext})=(S_{BET}–S_{micro}).[d] Total pore volume (V_{total}) estimated by the single point adsorption of pores according to Gurvich rule.[e] Micropore volume (V_{micro}) calculated by the t-plot method.[f] Mesopore volume (V_{meso})=(V_{total}–V_{micro}).

Table S5. Amount of acid sites obtained from the pyridine IR data.

Sample	*T*(K)	Brønsted acid umol/g	Lewis acid umol/g	B/L
USY-1	423	305.6	558.4	0.5
	523	258.6	141.0	1.8
	623	214.1	38.0	5.6
USY-2	423	54.7	313.7	0.2
	523	32.1	80.5	0.4
	623	22.4	11.3	2.0
USY-3	423	25.8	154.7	0.2
	523	14.1	51.2	0.3
	623	3.7	11.3	0.3
USY-4	423	27.2	170.6	0.2
	523	12.6	54.3	0.2
	623	5.5	4.8	1.1

Table S6. Comparison between the adsorption capacities of p-xylene on USY-3 and other adsorbents

Sorbents	Temp. / °C	Adsorption capacities (mg/g)	Si/Al	References
SPAO-5	Vapor 30	57.2	1: 20	3
ZnAPO-5	Vapor 25	192.2	---	4
FDU-15-350	Vapor 40	100.9	---	5
FDU-15-900	Vapor 40	234.6	---	5
Na-BETA	Liquid-batch 35	126.0	20	6
H/ZSM	Liquid breakthrough 170	142.2	> 450	7
NaY	Vapor 45	238.1	5	This work
USY-3	Vapor 45	292.1	94	This work

Table S7. Comparison between the adsorption capacities of m-xylene on USY-3 and other adsorbents

Sorbents	Temp. / °C	Adsorption capacities (mg/g)	Si/Al	References
SPAO-5	Vapor 30	54.3	1: 20	3
ZnAPO-5	Vapor 25	212.3	---	4
FDU-15-350	Vapor 40	98.7	---	5
FDU-15-900	Vapor 40	262.2	---	5
Na-BETA	Liquid-batch 35	71.0	20	6
H/ZSM	Liquid breakthrough 170	12.4	> 450	7
NaY	Vapor 45	229.1	5	This work
USY-3	Vapor 45	296.1	94	This work

References

1 Larson, A. C., & Von Dreele, R. B. General Structure Analysis System. Los Alamos National Laboratory Report LAUR 86-748 (Los Alamos National Laboratory, 1994).

2 Toby, B. H. EXPGUI, a graphical user interface for GSAS. J. Appl. Crystallogr. 2001, 34, 210–213.

3 E. Hu, Z. Lai and K. Wang, *Journal of Chemical & Engineering Data* 2010, **55**, 3286–3289.

4 S. Moulai, R. Ghezini, A. Hasnaoui, A. Benguedach and P. G. Weidler, *Research on Chemical Intermediates* 2019, **45**, 1653–1668.

5 Z. Wu, Y. Yang, B. Tu, P. A. Webley and D. Zhao, *Adsorption* 2009, **15**, 123–132.

6 A. Molaei Dehkordi and M. Khademi, *Microporous and Mesoporous Materials* 2013, **172**, 136–140.

7 M. Rasouli, N. Yaghobi, S. Chitsazan and M. H. Sayyar, *Microporous and Mesoporous Materials* 2012, **150**, 47–54.